Contents lists available at ScienceDirect

Journal of Inorganic Biochemistry

journal homepage: www.elsevier.com/locate/jinorgbio

Evaluation of heteroscorpionate ligands as scaffolds for the generation of Ruthenium(II) metallodrugs in breast cancer therapy

Elena Domínguez-Jurado [a,b], Consuelo Ripoll [a,c], Agustín Lara-Sánchez [b,*], Alberto Ocaña [d], Iñigo J. Vitórica-Yrezábal [e], Iván Bravo [a,c,*], Carlos Alonso-Moreno [a,b,*]

[a] *Universidad de Castilla-La Mancha, Unidad nanoDrug, Facultad de Farmacia de Albacete, 02008 Albacete, Spain*
[b] *Universidad de Castilla-La Mancha, Departamento de Química Inorgánica, Orgánica y Bioquímica, Facultad de Ciencias y Tecnologías Químicas-Centro de Innovación en Química Avanzada (ORFEO-CINQA), Ciudad Real 13071, Spain*
[c] *Universidad de Castilla-La Mancha, Departamento de Química Física. Facultad de Farmacia de Albacete, Albacete 02071, Spain*
[d] *Experimental Therapeutics Unit, Hospital clínico San Carlos, IdISSC and CIBERONC, Madrid, Spain*
[e] *Departamento de Química Inorgánica, Facultad de Ciencias, Universidad de Granada, Avda de Fuentenueva. s/n, 18071 Granada, Spain*

ARTICLE INFO

ABSTRACT

The modular synthesis of the heteroscorpionate core is explored as a tool for the rapid development of ruthenium-based therapeutic agents. Starting with a series of structurally diverse alcohol-NN ligands, a family of heteroscorpionate-based ruthenium derivatives was synthesized, characterized, and evaluated as an alternative to platinum therapy for breast cancer therapy. In vitro, the antitumoral activity of the novel derivatives was assessed in a series of breast cancer cell lines using UNICAM-1 and cisplatin as metallodrug control. Through this approach, a bimetallic heteroscorpionate-based metallodrug (RUSCO-2) was identified as the lead compound of the series with an IC$_{50}$ value range as low as 3–5 μM. Notably, RUSCO-2 was found to be highly cytotoxic in TNBC cell lines, suggesting a mode of action independent of the receptor status of the cells. As a proof of concept and taking advantage of the luminescent properties of one of the complexes obtained, uptake was monitored in human breast cancer MCF7 cell lines by fluorescence lifetime imaging microscopy (FLIM) to reveal that the compound is evenly distributed in the cytoplasm and that the incorporation of the heteroscorpionate ligand protects it from aqueous processes, conversion in another entity, or the loss of the chloride group. Finally, ROS studies were conducted, lipophilicity was estimated, the chloride/water exchange was studied, and stability studies in simulated biological media were carried out to propose structure-activity relationships.

1. Introduction

Heteroscorpionate ligands are intriguing, versatile, and robust polydentate compounds [1]. Due to their ease of structural modification, multiple coordinating sites, and large steric bulk, this type of ligands has been widely used as scaffolds to stabilize from early to late transition metals [2,3]. In fact, we have witnessed the incorporation of different types of anionic functional groups for many years, such as carboxylate, alkoxide, thiolate, aryloxide, sulphonate, cyclopentadienyl, or acetamidate in its structure, leading to novel features which broaden their scope of application [4]. Many catalytic processes have been investigated within the corresponding inorganic entities [3]. Group 4 heteroscorpionate catalysts have been mainly studied as catalyst precursors for olefin polymerization [5]. Some ruthenium heteroscorpionate catalysts

were designed to achieve ring-closing metathesis [6]. Likewise, ruthenium carbonyl derivatives were successfully tested as catalysts in the epoxidation of cyclohexene with different oxidizing agents [7]. Group 9 heteroscorpionate derivates provide an alternative to the Shilove approach for the alkane C—H bond activation [8]. Heteroscorpionate alkyl lanthanide catalysts displayed high catalytic activity in the hydroamination processes [9], and magnesium, zinc, and aluminium heteroscorpionate derivatives have been extensively described as very active initiators for the ring-opening polymerization of lactones and lactides [10–12]. Finally, aluminium heteroscorpionate complexes have also been shown very active catalysts for cyclic carbonate synthesis [13]. Furthermore, it was noted that a large amount of research has been devoted to the design and synthesis of metal complexes which structures mimic the active sites of metalloenzymes [14,15].

Despite these tridentate ligands represent a promising approach to stabilize metals in their low oxidations state, and therefore improve their adsorption and therapeutic activity, only a small number of studies have been reported in the field of oncology [4,14,15]. Compared to the platinum-based therapy in cancer: ruthenium complexes can be easily tuned from a six-coordination octahedron mode with a wide range of oxidation states leading to abundant metallodrug structures [16], analogously to iron, they can be transported in the blood through transferrin with faster absorption, metabolism and lower systemic toxicity [17]; their different mechanism of action may overcome resistances generated after platinum therapy [18,19]. There are a few ruthenium-based metallodrugs under clinical studies [20–22], and a plethora of them in preclinical studies as therapeutic agents for the treatment of breast cancer, ovarium cancer, and other common tumour types [23–25]. At present, these ruthenium complexes include distinct auxiliary ligands [26–28] and show different mechanisms of action, such as tumour growth inhibition, cell cycle arrest, apoptosis, autophagy, and generation of reactive oxygen species (ROS) [29]. From the pioneering work of Dyson et al. [30,31] in which RAPTA-C (see molecular structure in Fig. 1) was presented to explore ruthenium(II) in the search for other therapeutic alternatives to ruthenium(III) counterparts that made progress in clinical phases, such as NAMI-A[32] or KP1019 [33], a plethora of derivatives of RAPTA-C[26] [34–36] or the cyclopentadienyl-counterparts [37–39] have been reported. Proposals of structural–activity relationships are not evident. In this sense, the best outcomes were shown for those compounds maintaining the *p*-cymene moiety and tunning or replacing the 1,3,5-triaza-7-phosphaadamantane (PTA) auxiliary ligand. Thus, the water-soluble ruthenium(II) organometallic compound UNICAM-1 based on the bis(3,5 dimethylpyrazol-1-yl) methane ligand [40] (see molecular structure in Fig. 1), was evaluated in vivo against triple-negative breast cancer (TNBC) to report low toxicity and favourable clearance properties [41]. As far as we know, only a few heteroscorpionate-based ruthenium metallodrugs have been evaluated as an alternative to platinum therapy [42,43]. In this context, the versatility of the coordination mode of the heteroscorpionate ligands and their easily tunable core may provide exceptional and modulable steric and electronic features required for the rational design of new anticancer metallodrugs.

Breast cancer (BC) remains a worldwide health problem with >3.5 million cases expected in 2050. Therapies to treat this disease include the use of chemotherapy and targeted therapies, although the efficacy of many of them in practice is very limited due to the generation of resistance and the presence of adverse effects on the patient. Currently, there is no effective treatment for some subtypes of breast cancer, such as TNBC or HER2+ in advanced stages. Therefore, there is an urgent need to develop new effective therapeutic agents. In this regard, novel therapeutic alternatives based on ruthenium metallodrugs are actively being explored for the treatment of TNBC [37,44–47].
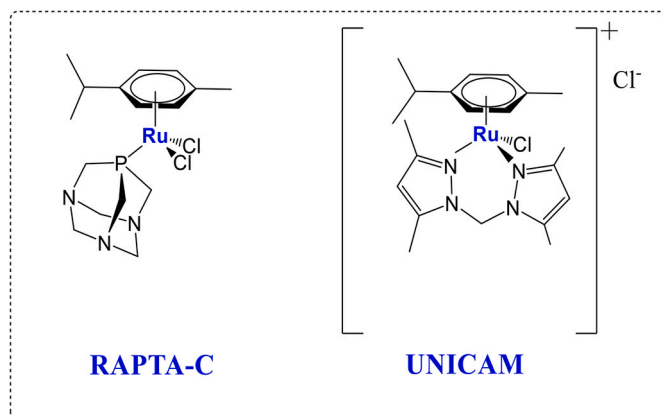
In this work, alcohol-based NN heteroscorpionate ligands have been assessed as auxiliary scaffolds for the generation of heteroscorpionate-based ruthenium derivatives. Due to the chemical robustness shown in previously reported organometallic analogues with this family of heteroscorpionate ligands [13,48], and the excellent antimetastatic properties showed by RAPTA derivatives in vivo [26], several RAPTA/heteroscorpionate hybrid ruthenium derivatives were designed, synthesized, and fully characterized by analytical, spectroscopic methods and X-ray crystallography studies. The novel complexes were tested against a panel of breast cancer tumoral cells and IC_{50} was calculated finding the leading agent of the series. The uptake was studied by time-resolved fluorescence microscopy of a fluorescent derivative.

2. Results and discussion

2.1. Synthesis and structural characterization of ruthenium compounds

Heteroscorpionate ligands L1-L5 were synthesized following the protocol previously reported for the synthesis of L1 and L2 [13]. After deprotonation at the methylene group of bis(3,5-dimethylpyrazol-1-yl) methane with Bu^{n}Li, an addition reaction with the corresponding aldehyde, the lithium salts were obtained as powered solids. The hydrolysis of the lithium salts with a saturated solution of NH$_4$Cl afforded the ligands L1-L5 as white or brown solids in good yields (ca. 80%) (Fig. 2). As expected, ^{1}H and ^{13}C{^{1}H} NMR spectra of L1-L5, exhibited two sets of resonances for the protons and carbons from the pyrazole rings, indicating they were not equivalent. These data were attributed to the presence of a chiral center in the C^a carbon of the ligand L1-L5 precursors (see Fig. S1-S6 in the Supporting Information). It should be noted that the L3 ligand incorporates an anthracene group that will provide optical properties to the ruthenium counterpart to facilitate uptake studies.

The proposed cationic ruthenium complexes (RUSCO-1-RUSCO-5) were obtained after stirring a mixture of the corresponding ligand and the ruthenium precursor [RuCl$_2$(*p*-cym)]$_2$ in MeOH/THF 3:1 (Fig. 3). The complex formation was monitored by ^{1}H NMR to be completed within a 4-h reaction time in all cases. RUSCO-1-RUSCO-5 were further purified by crystallization and were isolated in good yields (ca. 75%). These ruthenium complexes were soluble in DMSO and CH$_2$Cl$_2$ and showed minor solubility in water. Complexes were characterized spectroscopically (see Experimental Section and Fig. S7-S16 in the Supporting Information). The ^{1}H NMR and ^{13}C{^{1}H}-NMR spectra of these complexes showed two different sets of resonances for protons and carbons of both pyrazole rings, indicating they were not equivalent, the resonances for the different groups from the alcohol moiety, two different resonances for the methyl groups from the isopropyl moiety and the corresponding resonances for the *p*-cymene ring (Fig. 4). ^{1}H—^{1}H COSY experiments and ^{1}H—^{13}C heteronuclear correlation (g-HSQC) ascertained the assignment of most of the resonances (see Experimental Section and Fig. S17 in the Supporting Information). Based on spectroscopic data, ionic compounds are obtained with a chloride anion as a counterion and with a distorted-octahedral environment around the ruthenium centre in which the heteroscorpionate ligand is coordinated to the metal centre in a neutral κ^2-NN coordination mode (Fig. 3).

Single crystal X-ray diffraction studies for RUSCO-2 and RUSCO-3 confirmed the solid-state structure of ruthenium compounds. The corresponding ORTEP views are represented in Fig. 5. The crystallographic data and selected bond distances and angles are collected in Tables S1 and S2 in the Supporting Information, respectively. The molecular structures revealed a formally six-coordinated Ru(II) cation unit in which the ruthenium atom shows the typical "piano-stool" structure [49] with the metal centre coordinated to the heteroscorpionate ligand in a κ^2-NN coordination mode, a chloride atom, and the *p*-cymene group in a η^6-hapticity coordination mode (Fig. 5). The second chlorine atom appears as a counterion forming a hydrogen bond with the hydroxyl moiety of the heteroscorpionate ligand [O(1)-H(1)···Cl(2) 2.297 Å for
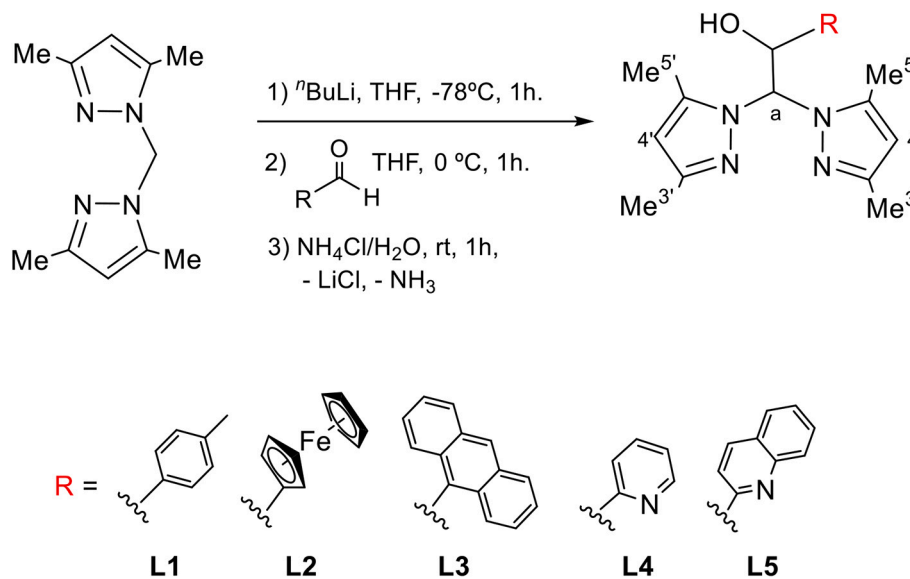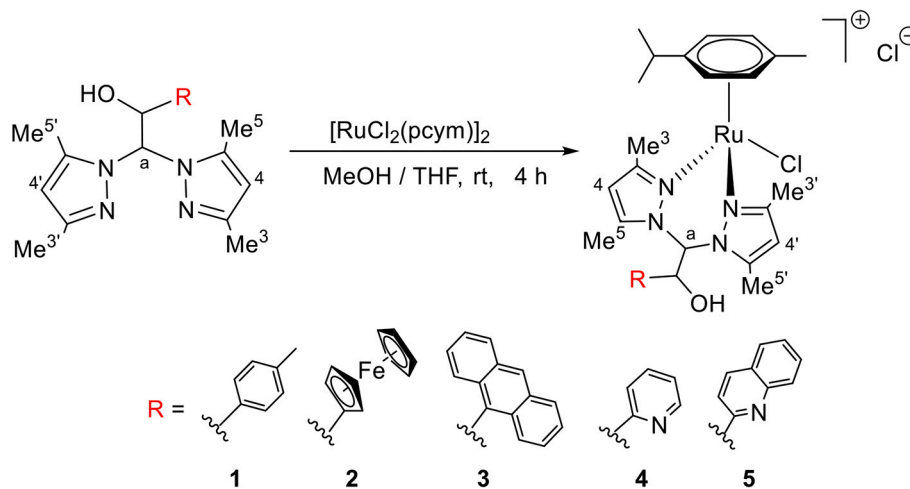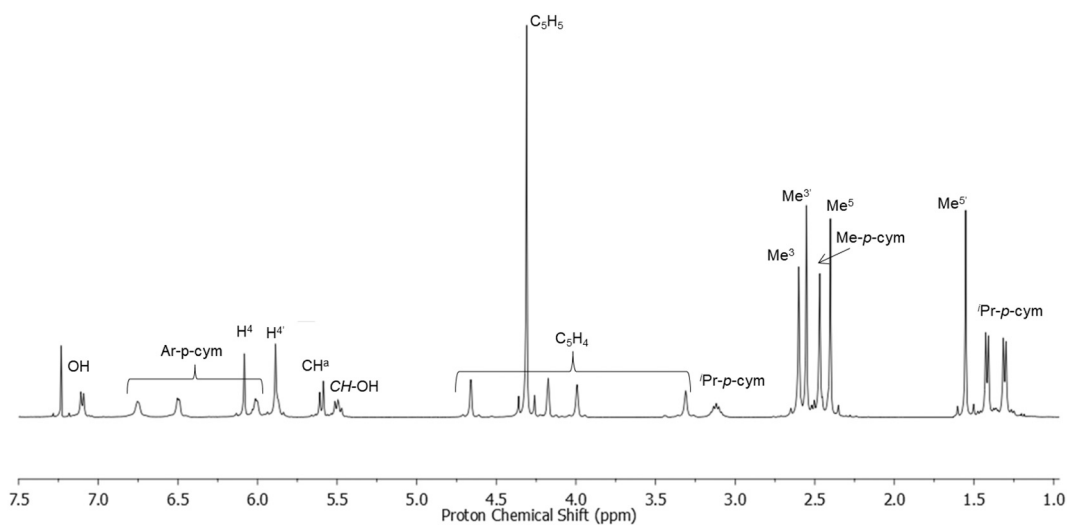

Fig. 1. Chemical structure of RAPTA-C and UNICAM-1 metallodrugs.

Fig. 2. Synthesis of precursors L1-L5.

Fig. 3. Synthesis of ruthenium-based agents (1–5). Yields ~80%.

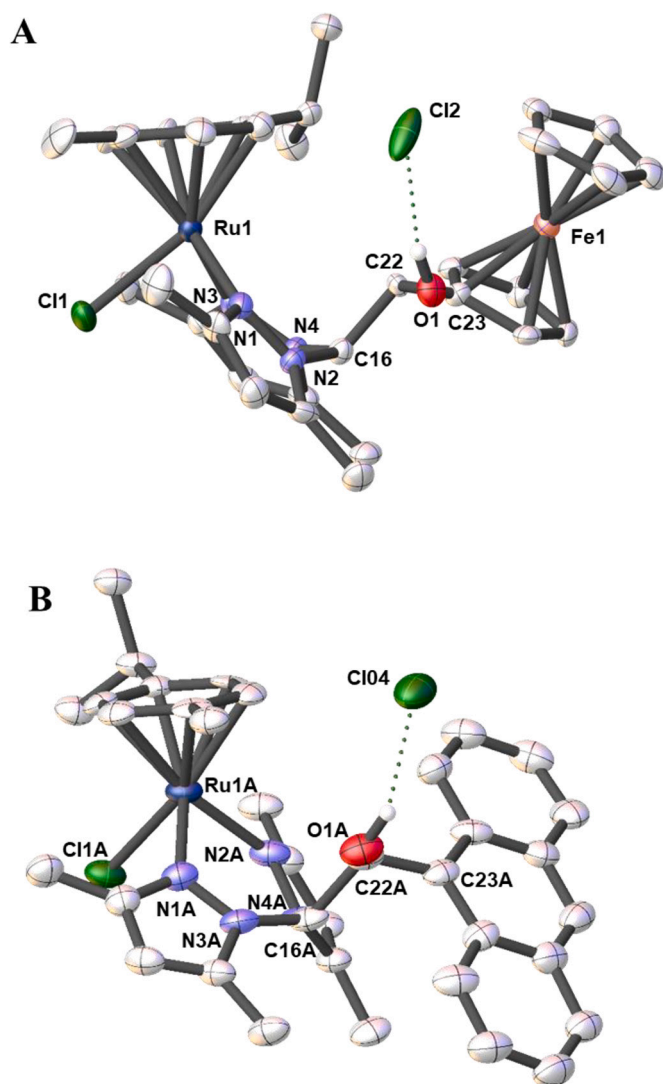**Fig. 4.** ^{1}HNMR spectrum of RUSCO-2 in CDCl$_3$.

Fig. 5. ORTEP plot in OLEX2 for the structure of RUSCO-2 (A) and RUSCO-3 (B). Thermal ellipsoids are given at the 30% probability level. All Hydrogen atoms have been omitted except for the OH for clarity. Ruthenium atoms are shown in dark blue, iron in orange, nitrogen in light blue, oxygen in red, chloride in green, and carbon and hydrogen in white. (For interpretation of the references to colour in this figure legend, the reader is referred to the web version of this article.)

RUSCO-2 and O(1 A)-H(1 A)···Cl(04) 2.266 Å for RUSCO-3]. RUSCO-2 crystallizes as an enantiopure complex in the chiral space group $P2_12_12_1$ and only shows the *S* enantiomer in the unit cell with a Flack parameter of −0.01(3), while RUSCO-3 crystallizes as a racemic mixture of both enantiomers in the asymmetric unit. The average Ru—N and Ru—Cl bond distances for both complexes are 2.119(9) Å and 2.410(2) Å, respectively, which are in good agreement with the literature data [32,33]. Bond angles confirmed the proposed "piano-stool" structure (See Table S2 in the Supporting Information).

2.2. Study of the stability of the ruthenium derivatives in aqueous media

The precursors L1-L5 were not soluble in water but the cationic complexes RUSCO-1-RUSCO-5 were air-stable, very soluble in chlorinated solvents and other polar solvents such as methanol and ethanol and have different solubility in water. Solubility in water has been measured by UV–vis spectroscopy. A calibration curve has been made for each compound and the solubility has been calculated using a saturated solution of the compounds. Then, according to the International Pharmacopeia [50,51], RUSCO-1 and RUSCO-4 are classified as soluble (35.06 mg/mL and 79.60 mg/mL, respectively), RUSCO-2 and RUSCO-3 are slightly soluble (6.84 mg/mL and 1.04 mg/mL, respectively) and RUSCO-5 is sparingly soluble (10.06 mg/mL). According to NMR experiments, ruthenium compounds degraded in chloroform after 72 h, generating a precipitate at the bottom of the NMR tube and affording a mixture of aromatic species from which the free *p*-cymene group was identified (see Fig. S18-S22 for RUSCO-1-RUSCO-5 in the Supporting Information). Metallodrugs are commonly dissolved in a mixture of DMSO:H_2O to perform biological assays which in any case did not exceed 0.25% *v*/v of DMSO. RAPTA complexes are prone to hydrolysis which is problematic for clinical evaluation trials. The stability of RUSCO-1-RUSCO-5, in DMSO-d_6:D_2O, $CDCl_3$ and simulated biological medium (DMSO-d_6:D_2O after adding NaCl), was monitored by NMR together with RAPTA-C as a control (see Fig. S18-S27 for RUSCO-1-RUSCO-5 and RAPTA-C stability in Fig. S29 of the Supporting Information). The set of signals belonging to RUSCO compounds persisted throughout stability experiments in contrast to RAPTA-C. The existence of only one pattern for the ruthenium derivatives discarded the fast chloride dissociation from RUSCO-1-RUSCO-5, contrary to that found for RAPTA-C. This was demonstrated by comparing the spectra before and after the addition of silver nitrate to the solution (see Fig. S28 for RUSCO-1, RUSCO-4, and RUSCO-5, as representative spectra) [52,53]. The silver nitrate forces the exchanged of the chloride moiety for one molecule of water. This generates the appearance of a precipitate (AgCl) and in turn, produces changes in the NMR spectrum. Therefore, the chelating ligand improves the stability of the ruthenium derivatives, while the arene group facilitates the uptake and interaction with potential targets. The loss of the arene group gives rise to ruthenium(III) derivatives and, therefore, causes an in-drop of antitumoral activity of the ruthenium metallodrugs. Tunning both building blocks may allow an improvement in the pharmacological profile of such a family of metallodrugs. Heteroscorpionate ligands are very well-known entities to stabilize early to late transition metals. From a chemical point of view, the robust nature of the heteroscorpionate ligand presents an ideal template for both high-throughput and rational metallodrug design. As it happens, the incorporation of such a robust ligand allowed an improvement in the stability of the ruthenium compounds.

On the other hand, differences in pharmacological profiles can be attributed to the ability of this family of compounds to penetrate biological membranes, which in turn is mainly dependent on lipophilicity factors. Calculated logarithmic octanol/water partition coefficients (clog P) [54] for RUSCO-1-RUSCO-5 were obtained using the software Molinsipiration (see Table S3 and Fig. S30 in the Supporting Information) [55]. The increasing size of the substituents on the heteroscorpionate scaffold might explain the observed lipophilicity pattern.

2.3. Antitumoral properties of ruthenium metallodrugs

The antitumoral properties of ruthenium complexes were evaluated in a panel of representative breast tumour cell lines including triple negative (BT549 and MDA-MB-231), HER2+ (SKBR3), and ER+/PR+ (MCF7) using UNICAM-1 and cisplatin as reference for metallodrugs. As can be seen in Fig. 6, most ruthenium compounds at 4 μM showed better antiproliferative effects than the reference ruthenium metallodrugs UNICAM-1, used as controls in all the cancer cell lines evaluated. RUSCO-2 was the most active ruthenium metallodrug of the series (see IC$_{50}$ values in Table 1 and dose-response curve for RUSCO-1, RUSCO-2, and RUSCO-3 in Fig. S31 in the Supporting Information). Ligands L1-L5 did not show significant cytotoxicity.

RUSCO-2 displayed higher cytotoxicity than cisplatin at low concentrations whereas increasing the doses makes both equipotent. These results indicate that tunning the core of the heteroscorpionate ligand led to a significant increase in the cytotoxicity of the resulting complexes. Notably, RUSCO-2 was found to be highly cytotoxic in TNBC cell lines,
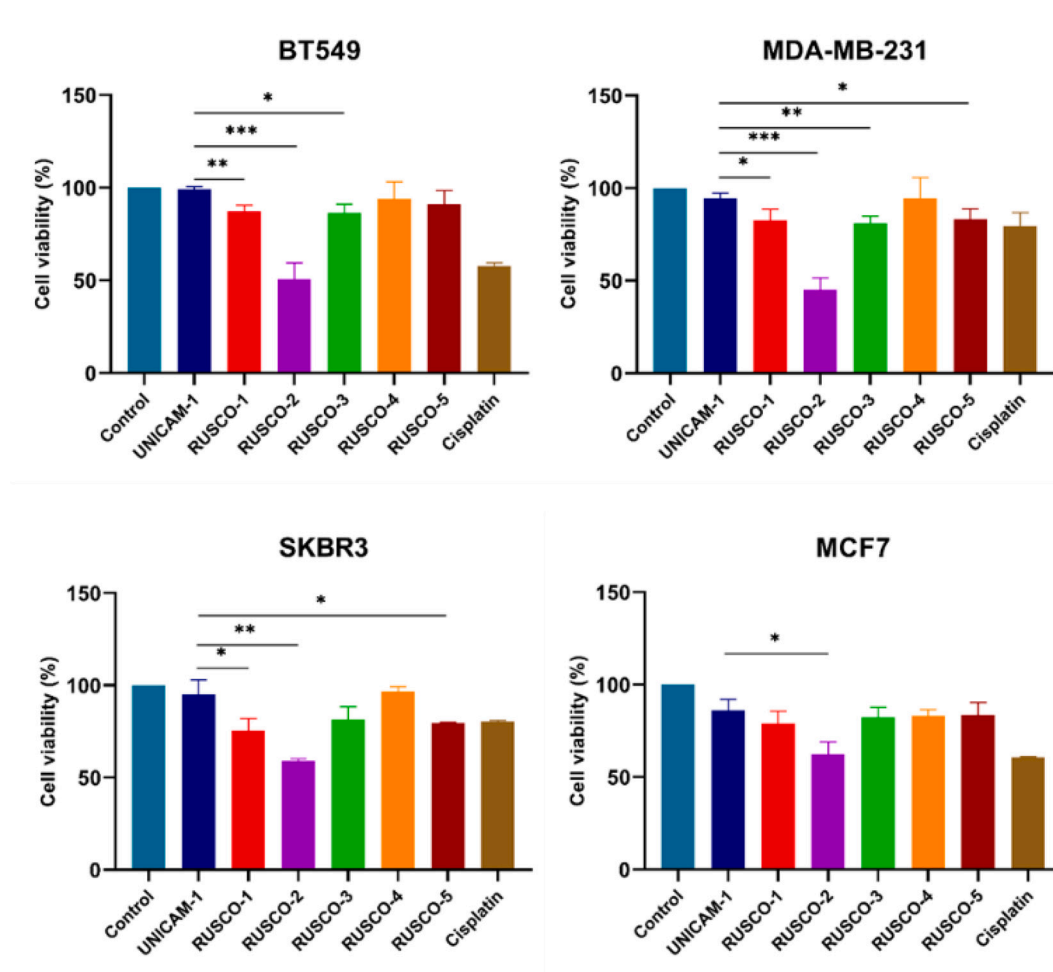
Fig. 6. Impact on cell viability of RUSCO-1-RUSCO-5, UNICAM-1, and cisplatin at 4 μM. (A) Screening of several ruthenium compounds by exploring cell viability in BT549, SKBR3, MDA-MB-231, and MCF7 breast cancer cell lines for 72 h evaluated using MTTs. Data are the average $+/-$ standard deviation (SD) of three independent experiments performed in triplicate. To determine significant statistical differences, a Student's t-test was used. The values for the statistical analyses are * $p \leq 0.05$; ** $p \leq 0.01$; *** $p \leq 0.001$.

Table 1
IC$_{50}$ values for ruthenium complexes in a panel of breast cancer tumour cells.[a]

Cell Line	IC$_{50}$ values (μM)						
	RUSCO-1	RUSCO-2	RUSCO-3	RUSCO-4	RUSCO-5	UNICAM-1	Cisplatin
BT549	14.20 ± 1.39	3.45 ± 0.45	13.93 ± 0.77	>20	>20	>20	5.50 ± 0.28
MDA-MB-231	12.79 ± 0.64	3.19 ± 0.76	12.85 ± 1.68	>20	14.53 ± 2.49	>20	11.14 ± 1.55
SKBR3	8.50 ± 0.50	4.07 ± 2.10	9.57 ± 1.24	>20	16.30 ± 1.43	>20	6.69 ± 0.65
MCF7	13.63 ± 0.57	5.10 ± 0.20	12.93 ± 1.89	18.24 ± 0.87	15.68 ± 0.17	>20	10.12 ± 2.10
HaCaT	–	3.36 ± 0.20	–	–	–	>20	2.01 ± 0.04
HEK-293	–	5.40 ± 1.64	–	–	–	>20	11.86 ± 2.29

[a] Values are means $\pm$ SDs obtained by the MTT assay (exposure time: 72 h).

suggesting a mode of action independent of the receptor status of the cells. TNBC lacks effective treatments, with a five-year survival rate of 20–90% depending on its stage [56]. The clinical relevance of TNBC entails the need to explore other alternatives to address this disease: improve existing treatments or generate new drugs [28].

The toxicity in non-transformed cells was also evaluated in vitro (Table 1). To do so, the non-transformed but immortalized keratinocyte cell line HaCaT and the immortalized human embryonic kidney cell line HEK 293, as a proof of concept, were treated with only the lead compound of the series and using cisplatin as the reference metallodrug. RUSCO-2, as the lead compound of the series, did not reduce the toxicity of cisplatin showed in non-tumoral cells (see Fig. 7 and Table 1).

2.4. Reactive Oxygen Species (ROS) generation by RUSCO compounds

Metal complexes can directly or indirectly alter the cellular redox balance through redox pathways. Consequently, studies on reactive oxygen species (ROS) generation have been carried out to ascertain whether the observed antitumor activity could be attributed to redox reactions [15]. The assessment of ROS generation by RUSCO-1-RUSCO-5 was conducted in the MCF7 breast cancer cell line, using H_2O_2 as a positive control. All the complexes were tested at a concentration of 3 μM. As depicted in Fig. 8, none of the compounds generated ROS compared to the negative control. Therefore, the superior activity of compound RUSCO-2 is not attributed to ROS generation.
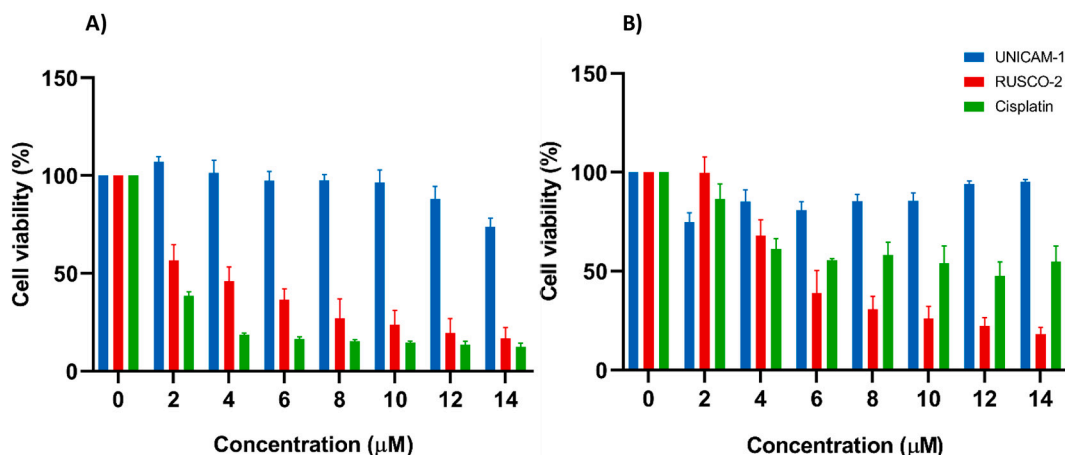
Fig. 7. Impact on cell viability of RUSCO-2 and cisplatin in non-transformed HaCaT cells (A) and in an immortalized human embryonic kidney cell line, HEK 293 (B), for 72 h evaluated using MTTs. Data are the average +/− standard deviation (SD) of three independent experiments performed in triplicate.
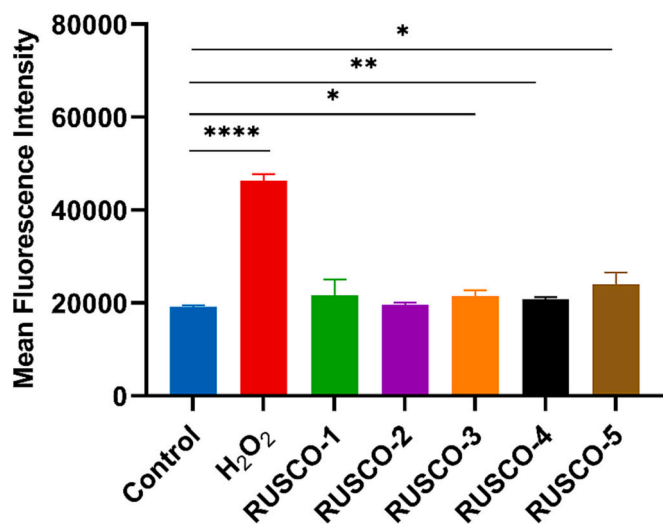

Fig. 8. Mean Fluorescence Intensity as a quantification of ROS generation by RUSCO-1-RUSCO-5 and comparing it to H_2O_2 as a positive control. Data are the average +/− standard deviation (SD) of three independent experiments performed in triplicate. To determine significant statistical differences, a Student's *t*-test was used. The values for the statistical analyses are * $p \leq 0.05$; ** $p \leq 0.01$; *** $p \leq 0.001$; **** $p \leq 0.0001$.

2.5. Uptake studies for RUSCO compounds

Taking advantage of the fact that RUSCO-3 displays luminescent properties, this compound was monitored in human breast cancer MCF7 cell lines by fluorescence lifetime imaging microscopy (FLIM) as a proof of concept to gain insight into their mechanism of action (Fig. 9). First, the photophysical behavior of L3 and RUSCO-3 was studied. Fig. 9A and S34 shows the absorbance and fluorescence spectra of this complex and its ligand in pH 7.4 PBS buffer. The electronic absorption spectrum shows high energy contributions within 200–300 nm with a well-defined intense band centred at 257 nm that can be assigned to intra-ligand $\pi \rightarrow \pi^*$ and $n \rightarrow \pi^*$ transitions from heteroscorpionate and *p*-cymene ligands [57]. The typical spectrum of anthracene with vibronic structure can be observed at 370 nm, whereas no MLCT transitions at low energies are observed [58]. In such a way that the fluorescence spectrum corresponds exclusively to the emission of the anthracene ligand as an independent entity: a mirror image emission spectrum within 370–600 nm where the vibronic structure is easily appreciated.

Thus, the dynamic behavior of RUSCO-3 shows a monoexponentially decay upon excitation at 368 nm leading to a fluorescence lifetime of 9.76 ns, see Fig. 9B, which make it easy to monitor by FLIM. Such microscopy is an excellent tool to monitor both cellular uptake and intracellular diffusion of fluorescent drugs because of the high sensitivity of fluorescence lifetimes to the local environment, as well as to possible chemical transformations that drugs or pre-drugs may undergo. Being very useful to follow action mechanisms and intracellular localization in compartments and/or organelles. The FLIM images of MCF7 cell line following at 1, 2, 4, 8, 24 and 48-h incubation (Fig. 9C) demonstrate the rapid internalization and excellent stability in the biological environment of RUSCO-3. The compound is observed exclusively in the cytoplasm from the first hour of incubation and is not present in the nucleus at longer times. However, in the images, a certain accumulation is observed in very specific areas within the cytoplasm suggesting two different populations of RUSCO-3 coexisting.

To begin with the histogram analysis, the overall average lifetime distribution for all the cell lines is narrow and spans from 5 to 12.5 ns. No differences are observed in the histograms at different incubation times, all being centered around 8.3 ns. Detailed analysis of the lifetime distribution histograms requires two Gaussian functions for an accurate fit, which suggests that RUSCO-3 is present in different forms in the cell environment (Fig. 9D and S32 in the Supporting Information). The deconvolution shows that the dominant contribution arises from a population of RUSCO-3 molecules with lifetimes of 5–10 ns, with an average lifetime centered at 8.1 ns (55%) and appears homogeneously distributed within the cytoplasm. On the other hand, the maximum value of the lifetime for the second population is significantly different: ~9 ns centered and shifted up to 12.5 ns (45%). This shift to longer lifetimes suggests a more hydrophobic environment for this second population [59], which are represented as sub-micron aggregates in the images, probably due to accumulation in lipid droplets, endoplasmic reticulum via interactions with macromolecules, or mitochondria.

To clarify the nature of these accumulations of RUSCO-3 with a hydrophobic environment inside, cell colocalization experiments were performed. MCF7 cells were treated with a specific mitochondrial dye (mitotracker) capable of exclusively staining the mitochondria. Thus, we can excite both RUSCO-3 and the mitotracker to obtain simultaneous colocalization. Fig. 9E shows the images when the mitrotracker and RUSCO-3 are excited separately and when both merges. The results show that mitochondria are not the preferred site of accumulation. Finally, further analysis in the nucleus and cytoplasm as a region of interest shows that lifetime distribution histogram shifts to lower average lifetime values (7.7 ns) in the nucleus when compared to the cytoplasm (8.3 ns), and besides that, RUSCO-3 population is practically
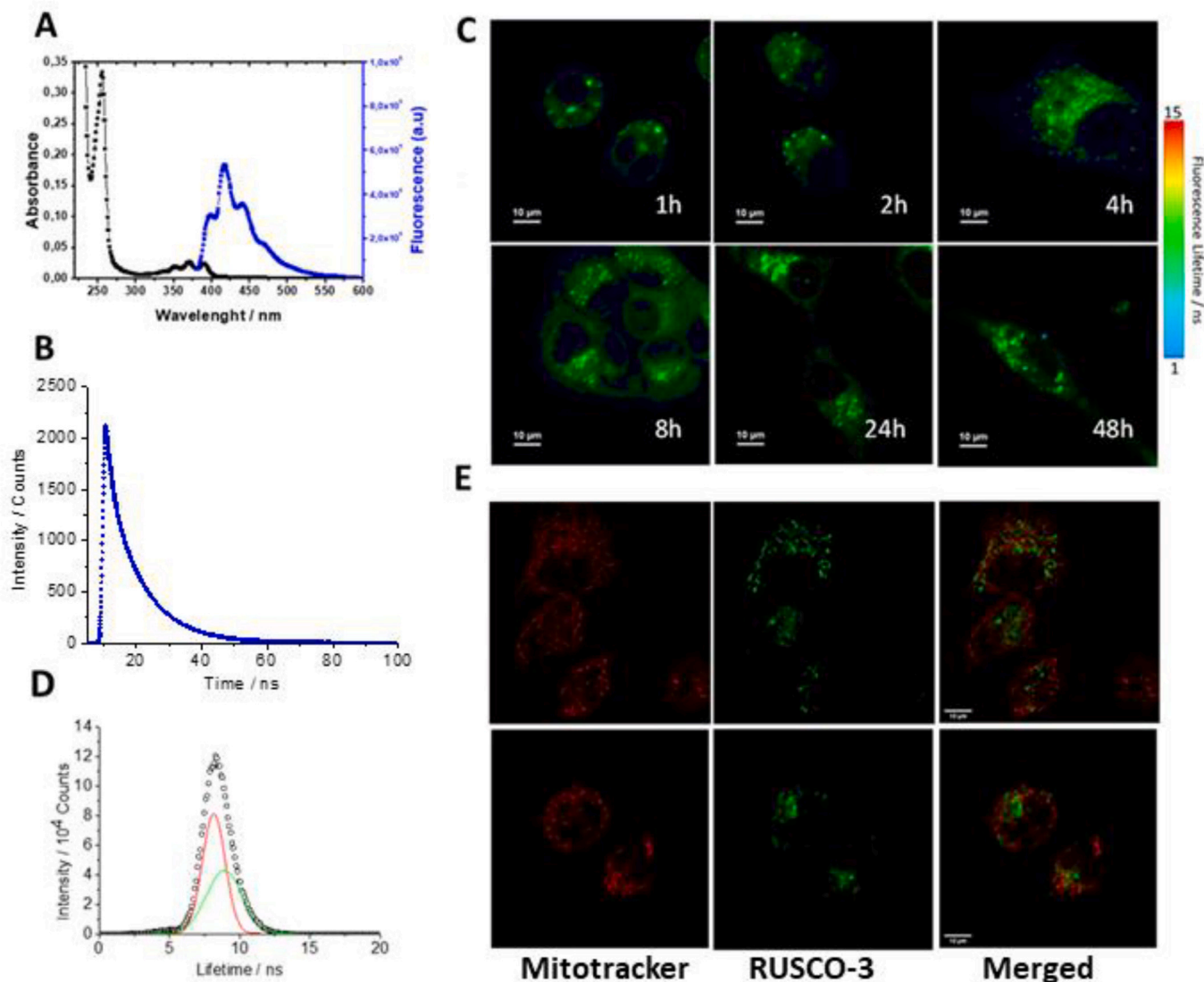
Fig. 9. A) Absorption and emission spectra of RUSCO-3 pH 7.4 PBS buffer. B) Fluorescent decay profile of RUSCO-3 in pH 7.4 PBS buffer. C) FLIM images of MCF7 cell lines after treatment with RUSCO-3 at different times (1 h - 48 h). D) Overall histogram and deconvolution of the average emission lifetimes (1 h – 48 h) collected as average of each FLIM images. E) MCF7 cell treated with mitotracker, RUSCO-3, and merged.

negligible in the nucleus when compared to the cytoplasm (7% vs. 93%) according to the areas of the respective histograms (see Fig. S33).

3. Experimental section

3.1. Synthesis and characterization

3.1.1. General procedure

Synthesis reactions were performed using standard Schlenk and glove-box techniques under an atmosphere of dry nitrogen. THF and hexane were pre-dried over sodium wire and distilled under nitrogen. CDCl$_3$, DMSO-d_6, and D$_2$O were stored over activated 4 Å molecular sieves and degassed by several freeze-thaw cycles. All NMR experiments were conducted in deuterated solvents at 297 K in a Varian FT-400 spectrometer (VARIAN Inc., Palo Alto city, California, USA) equipped with a 4 nucleus ASW PFG ^{1}H/^{19}F/^{13}C/{^{15}N–^{31}P}. The 1H $\pi/2$ pulse length was adjusted for each sample. ^{1}H- and ^{13}C{^{1}H}-NMR chemical shifts (δ) are given in ppm relative to TMS. Coupling constants (J) are documented in Hz. The solvent signals were used as references and chemical shifts were converted to the TMS scale. IR experiments were conducted on an FT/IR-4000 series Jasco instruments (Jasco analytics,

Madrid, Spain). The UV–vis absorption spectra were recorded at room temperature using a Cary 100 spectrophotometer (Agilent, Madrid, Spain) using a slit width of 0.4 nm and a scan rate of 600 nm/min. Microanalyses were performed with a PerkinElmer 2400 CHN analyzer

3.1.2. Synthesis and characterization of ligands L1-L5

To a solution of bis(3,5-dimethyl-1*H*-pyrazol-1-yl)methane (2.00 g, 9.77 mmol) in THF (50 mL) at −78 °C was added dropwise *n*-butyl-lithium 1.6 M (6.11 mL, 9.77 mmol). After 1 h stirring time under N$_2$ atmosphere, the solution was transferred via cannula to another Schlenk containing the corresponding aldehyde (9.79 mmol), and the mixture was allowed to stir for 1 h at room temperature. An aqueous saturated NH$_4$Cl solution (50 mL) was added to protonate the ligand. After extracting the organic phase and removing the solvent under vacuum, the resultant solid was washed with *n*-hexane. Filtration of the precipitate afforded a yellowish solid. L1 and L2 were synthesized following the procedure described in the literature.[13]

3.1.3. 1-(anthracen-9-yl)-2,2-bis(3,5-dimethyl-1H-pyrazol-1-yl)ethan-1-ol (bpzanteH; L3)

Yield: 3.26 g, 7,86 mmol, 80%. ^{1}H NMR (400 MHz, CDCl$_3$) δ:

9.50–7.24 (set of bs, 9H, anthracene group, 7.46 (d, J_{HH} = 8.9 Hz, 1H, CH^a), 6.79 (d, J_{HH} = 8.9 Hz, 1H, CH-OH), 5.94 (s, 1H, H^4), 5.47 (s, 1H, OH), 5.01 (s, 1H, H$^{4'}$), 2.38 (s, 3H, Me^3), 1.96 (s, 3H, Me$^{3'}$), 1.95 (s, 3H, Me^5), 0.89 (s, 3H, Me$^{5'}$). ^{13}C{^{1}H}- NMR (101 MHz, CDCl$_3$) δ: 149.1–120.0 (C$^{3,3'}$, C$^{5,5'}$ and carbon from anthracene group), 106.8 (C^4), 104.9 (C$^{4'}$), 70.8 (*C*H-OH), 70.4 (C^a), 14.0 (Me^3), 13.8 (Me$^{3'}$), 10.8 (Me^5), 9.5 (Me$^{5'}$). UV–vis: two maximum absorbances at 255 and 207 nm. Elemental analysis calculated (%) for C$_{26}$H$_{26}$N$_4$O: C, 76.07; H, 6.38; N, 13.65; found: C, 76.16; H, 6.41; N, 13.46.

3.1.4. 2,2-bis(3,5-dimethyl-1H-pyrazol-1-yl)-1-(pyridin-2-yl)ethan-1-ol (bpzpyeH; L4)

Yield: 2.47 g, 7.92 mmol, 81%. ^{1}H NMR (400 MHz, CDCl$_3$) δ 8.56 (d, J_{HH} = 4.8 Hz, 1H, CH^6 pyridine), 7.51 (m, J_{HH} = 7.7 Hz, 1H, CH^4 pyridine), 7.16 (m, 1H, CH^5 pyridine), 7.07 (d, *J* = 7.8 Hz, 1H, CH^3 pyridine), 6.44 (d, *J* = 6.6 Hz, 1H, CH^a), 5.93 (d, *J* = 6.6 Hz, 1H, CH-OH), 5.77 (s, 1H, H^4), 5.63 (s, 1H, H$^{4'}$), 5.36 (s, 1H, OH), 2.20 (s, 3H, Me^3), 2.17 (s, 3H, Me$^{3'}$), 2.07 (s, 3H, Me^5), 1.93 (s, 3H, Me$^{5'}$). ^{13}C{^{1}H}- NMR (101 MHz, CDCl$_3$) δ 157.7 (C^2 pyridine), 148.7 (C^6 pyridine), 148.6, 148.3, 140.5, 139.7(C$^{3,3'}$, C$^{5,5'}$), 136.5 (C^4 pyridine), 123.0 (C^5 pyridine), 122.5 (C^3 pyridine), 106.4 (C^4), 105.9 (C$^{4'}$), 74.9 (C^a), 72.4 (*C*H-OH), 13.7 (Me^3), 13.7 (Me$^{3'}$), 10.9 (Me^5), 10.6 (Me$^{5'}$). UV–vis: maximum absorbance at 207 nm. Elemental analysis calculated (%) C$_{17}$H$_{21}$N$_5$O: C, 65.57; H, 6.80; N, 22.49; found: C, 65.61; H, 6.83; N, 22.11.

3.1.5. 2,2-bis(3,5-dimethyl-1H-pyrazol-1-yl)-1-(quinolin-2-yl)ethan-1-ol (bpzqeH; L5)

Yield: 2.53 g, 7.01 mmol, 72%. ^{1}H NMR (400 MHz, CDCl$_3$) δ 8.09 (d, *J* = 8.5 Hz, 1H, CH^8 quinoline), 8.00 (d, J_{HH} = 8.5 Hz, 1H, CH^3 quinoline), 7.78 (d, J_{HH} = 8.1 Hz, 1H, CH^5 quinoline), 7.71 (m, 1H, CH^7 quinoline), 7.53 (m, 1H, CH^6 quinoline), 7.18 (d, J_{HH} = 8.5 Hz, 1H, CH^4 quinoline), 6.59 (d, J_{HH} = 6.8 Hz, 1H, CH^a), 6.12 (s, 1H, CH-OH), 5.78 (s, 1H, H^4), 5.64 (s, 1H, H$^{4'}$), 5.60 (s, 1H, OH), 2.22 (s, 3H, Me^3), 2.20 (s, 3H, Me$^{3'}$), 2.15 (s, 3H, Me^5), 1.92 (s, 3H, Me$^{5'}$). ^{13}C{^{1}H}-NMR (101 MHz, CDCl$_3$) δ 159.1–110.0 (C$^{3,3'}$, C$^{5,5'}$ and carbon from quinoline group), 106.5 (C^4), 106.1 (C$^{4'}$), 75.0 (*C*H-OH), 72.6 (C^a), 13.8 (Me$^{3,3'}$), 11.1 (Me^5), 10.7 (Me$^{5,5'}$). UV–vis: maximum absorbance at 207 nm. Elemental analysis calculated (%) for C$_{21}$H$_{23}$N$_5$O: C, 69.78; H, 6.41; N, 19.38; found C, 69.88; H, 6.66; N, 19.23.

3.1.6. Synthesis and characterization of ruthenium compounds RUSCO-1-RUSCO-5

The ruthenium dimer [RuCl$_2$(*p*-cym)]$_2$ (0.25 mmol, 0.15 g) was dissolved in MeOH/THF 3:1 and stirred for 30 min. The corresponding ligand (0.50 mmol) was added to the red solution and the mixture was allowed to stir for 4 h at room temperature and under N$_2$ atmosphere. The colour of the solution shifted from red to orange. The solvent was removed under vacuum and the residual power was washed with diethylether (5 mL) and then with *n*-hexane (10 mL). The solid was dried under vacuum providing the ruthenium complexes as orange solids. UNICAM-1 was synthesized following the procedure described in the literature [40].

3.1.7. [RuCl(κ^2-NN-bpzteH)(p-cym)][Cl] (RUSCO-1)

Yield: 0.253 g, 0.40 mmol, 80%. ^{1}H NMR (400 MHz, CDCl$_3$) δ 7.02 (d, J_{HH} = 7.7 Hz, 2H, *p*-tolyl), 6.95 (d, J_{HH} = 8.0 Hz, 2H, *p*-tolyl), 6.50 (brs, 1H, CH^a), 6.23 (d, J_{HH} = 5.8 Hz, 1H, Ar-*p*-cym), 6.12 (s, 1H, H^4), 6.02 (d, J_{HH} = 5.9 Hz, 1H, Ar-*p*-cym), 5.90 (brs, 2H, H$^{4'}$ and 1H Ar-*p*-cym), 5.82 (brs, 1H, Ar-*p*-cym), 5.69 (d, J_{HH} = 9.6 Hz, 1H, CH-OH), 3.16 (m, 1H, ^{i}Pr-*p*-cym), 2.65 (s, 3H, Me^3), 2.58 (s, 3H, Me$^{3'}$), 2.44 (s, 3H, Me^5), 2.37 (s, 3H, Me-*p*-cym), 2.28 (s, 3H, Me-*p*-tolyl), 1.34 (s, 3H, Me$^{5'}$), 1.32 (d, J_{HH} = 2.7 Hz, 3H, ^{i}Pr-*p*-cym), 1.30 (d, J_{HH} = 2.7 Hz, 3H, ^{i}Pr-*p*-cym). ^{13}C{^{1}H}-NMR (101 MHz, CDCl$_3$) δ: 156.9–125.0 (C$^{3,3'}$, C$^{5,5'}$, quaternary carbons of *p*-cym and carbons of Ar-*p*-tolyl), 110.0, 109.4 (C$^{4,4'}$), 100.3, 86.4, 85.7, 81.1 (*Ar*-*p*-cym), 72.7 (C^a), 70.8 (CH-OH), 31.3

(CH, ^{i}Pr-*p*-cym), 23.3 (Me, ^{i}Pr-*p*-cym), 22.7 (Me, ^{i}Pr-*p*-cym), 21.1 (Me, *p*-cym), 18.8 (Me^3), 17.4 (Me$^{3'}$), 17.1 (Me, *p*-tolyl), 12.3 (Me^5), 10.9 (Me^5). UV–vis: maximum absorbance at 207 nm. Elemental analysis calculated (%) for C$_{29}$H$_{38}$Cl$_2$N$_4$ORu: C, 55.23; H, 6.07; N, 8.88 found C, 55.30; H, 6.26; N, 8.71.

3.1.8. [RuCl(κ^2-NN-bpzFerrH)(p-cym)][Cl] (RUSCO-2)

Yield: 0.28 g, 0.38 mmol, 79%. ^{1}H NMR (400 MHz, CDCl$_3$) δ: 7.10 (d, J_{HH} = 7.0 Hz, 1H, OH), 6.75 (brs, 1H, Ar-*p*-cym), 6.50 (brs, 1H, Ar-*p*-cym), 6.08 (s, 1H, H^4), 6.01 (brs, 1H, Ar-*p*-cym), 5.89 (s, 1H, H$^{4'}$), 5.85 (brs, 1H, Ar-*p*-cym), 5.60 (d, J_{HH} = 9.5 Hz, 1H, CH^a), 5.49 (m, 1H, CH-OH), 4.66 (s, 1H, C$_5$H$_4$), 4.31 (s, 5H, C$_5$H$_5$), 4.17 (s, 1H, C$_5$H$_4$), 3.99 (s, 1H, C$_5$H$_4$), 3.31 (s, 1H, C$_5$H$_4$), 3.12 (m, 1H, ^{i}Pr-*p*-cym), 2.60 (s, 3H, Me^3), 2.55 (s, 3H, Me$^{3'}$), 2.47 (s, 3H, Me^5), 1.55 (s, 3H, Me$^{5'}$), 1.42 (d, J_{HH} = 6.7 Hz, 3H, ^{i}Pr-*p*-cym), 1.31 (d, J_{HH} = 6.7 Hz, 3H, ^{i}Pr-*p*-cym). ^{13}C{^{1}H}-NMR (101 MHz, CDCl$_3$) δ: 156.5–125.8 (C$^{3,3'}$, C$^{5,5'}$ and quaternary carbons of *p*-cym), 110.0, 109.5 (C$^{4,4'}$), 110.8–80.0 (Ar-*p*-cym), 72.9 (C^a), 69.2 (*C*$_5$H$_5$ and CH-OH), 68.3–65.8 (*C*$_5$H$_4$), 31.3 (CH, ^{i}Pr-*p*-cym), 23,4, 23.1 (Me, ^{i}Pr-*p*-cym), 18.9 (Me, *p*-cym), 17.4 (Me^3), 17.2 (Me$^{3'}$), 12.5 (Me^5), 11.6 (Me$^{5'}$). UV–vis: maximum absorbance at 207 nm. Elemental analysis calcd (%) for C$_{32}$H$_{40}$Cl$_2$FeN$_4$ORu: C, 55.78; H, 5.85; N, 8.13; found C, 55.84; H, 5.90; N, 8.04.

3.1.9. [RuCl(κ^2-NN-bpzanteH)(p-cym)][Cl] (RUSCO-3)

Yield: 0.29 g, 0.41 mmol, 82%. ^{1}H NMR (400 MHz, CDCl$_3$) δ: 9.61–6,49 (m, 9H, anthracene group), 7.96 (d, J_{HH} = 8.4 Hz, 1H, CH-OH), 7.44 (d, J_{HH} = 8.0 Hz, 1H, CH^a), 6.98 (brs, 1H, Ar-*p*-cym), 6.34 (d, J_{HH} = 5.7 Hz, 1H, Ar-*p*-cym), 6.22 (s, 1H, H^4), 6.05 (d, J_{HH} = 5.1 Hz, 1H, Ar-*p*-cym), 5.96 (d, J_{HH} = 5.5 Hz, 1H, Ar-*p*-cym), 5.00 (s, 1H, H$^{4'}$), 3.27 (m, 1H, ^{i}Pr-*p*-cym), 2.70 (s, 3H, Me^3), 2.64 (s, 3H, Me$^{3'}$), 2.30 (s, 3H, Me-*p*-cym), 2.27 (s, 3H, Me^5), 1.46 (d, J_{HH} = 6.6 Hz, 3H, ^{i}Pr-*p*-cym), 1.20 (d, J_{HH} = 6.9 Hz, 3H, ^{i}Pr-*p*-cym), 0.38 (s, 3H, Me$^{5'}$). ^{13}C{^{1}H}-NMR (101 MHz, CDCl$_3$) δ: 158.3, 156.5, 147.3, 145.4 (C$^{3,3'}$, C$^{5,5'}$), 131.7–125.2 (carbons from anthracene group and quaternary carbons of *p*-cym), 110.8–80.0 (Ar-*p*-cym), 110.6 (C^4), 108.6 (C$^{4'}$), 71.2 (*C*H-OH), 70.7 (C^a), 32.0 (CH, ^{i}Pr-*p*-cym), 24.2, 21.8 (Me, ^{i}Pr-*p*-cym), 18.5 (Me, *p*-cym), 17.4 (Me^3), 16.9 (Me$^{3'}$), 13.3 (Me^5), 9.8 (Me$^{5'}$). UV–vis: maximum absorbance at 207 nm. Elemental analysis calculated (%) for C$_{36}$H$_{40}$Cl$_2$N$_4$ORu: C, 63.47; H, 5.92; N, 8.22; found C, 63.52; H, 6.08; N, 8.19.

3.1.10. [RuCl(κ^2-NN-bpzpyeH)(p-cym)][Cl] (RUSCO-4)

Yield: 0.25 mg, 0.40 mmol, 80%. ^{1}H NMR (400 MHz, CDCl$_3$) δ: 8.27 (d, J_{HH} = 4.0 Hz, 1H, pyridine group), 8.04 (d, J_{HH} = 7.9 Hz, 1H, pyridine group), 7.74 (m, 1H, pyridine group), 7.29 (d, J_{HH} = 5.9 Hz, 1H, CH^a), 7.15 (dd, J_{HH} = 7.4, 4.9 Hz, 1H, pyridine group), 6.46 (d, J_{HH} = 6.2 Hz, 1H, Ar-*p*-cym), 6.29 (d, J_{HH} = 6.2 Hz, 1H, Ar-*p*-cym), 6.10 (m, 4H, Ar-*p*-cyme, H^4, CHOH), 5.85 (s, 1H, H$^{4'}$), 3.13 (m, 1H, ^{i}Pr-*p*-cym), 2.60 (s, 3H, Me^3), 2.59 (s, 3H, Me$^{3'}$), 2.46 (s, 3H, Me-*p*-cym), 2.38 (s, 3H, Me^5), 1.62 (s, 3H, Me$^{5'}$), 1.23 (d, J_{HH} = 6.8 Hz, 3H, ^{i}Pr-*p*-cym), 1.16 (d, J_{HH} = 6.8 Hz, 3H, ^{i}Pr-*p*-cym). ^{13}C{^{1}H}-NMR (101 MHz, CDCl$_3$) δ: 158.8–122.8 (C$^{3,3'}$,C$^{5,5'}$, pyridine group and quaternary carbons of *p*-cym), 109.7 (C^4), 109.3 (C$^{4'}$), 110.5–80.0 (Ar-*p*-cym), 71.6 (*C*H-OH), 70.9 (C^a), 31.3 (CH, ^{i}Pr-*p*-cym), 24.1, 23.2 (Me, ^{i}Pr-*p*-cym), 18.6 (Me, *p*-cym), 17.2 (Me^3), (Me$^{3'}$), 12.4 (Me^5), 11.2 (Me$^{5'}$). UV–vis: maximum absorbance at 207 nm. Elemental analysis calculated (%) for C$_{27}$H$_{35}$Cl$_2$N$_5$ORu: C, 52.51; H, 5.71; N,11.34; found C, 52.67; H, 5.82; N, 11.22.

3.1.11. [RuCl(κ^2-NN-bpzqeH)(p-cym)][Cl] (RUSCO-5)

Yield: 0.29 g, 0.43 mmol, 86%. ^{1}H NMR (400 MHz, CDCl$_3$) δ: 8.22–7.52 (m, 6H, quinoline group), 6.62 (d, J_{HH} = 5.1 Hz, 1H, Ar-*p*-cym), 6.35 (d, J_{HH} = 5.6 Hz, 1H, Ar-*p*-cym), 6.28 (brs 2H, CH-OH and CH^a), 6.13 (s, 1H, H^4), 6.10 (d, J_{HH} = 5.7 Hz, 1H, Ar-*p*-cym), 6.07 (d, J_{HH} = 5.2 Hz, 1H, Ar-*p*-cym), 5.87 (s, 1H, H$^{4'}$), 3.14 (m, 1H, ^{i}Pr-*p*-cym), 2.64 (s, 3H, Me^3), 2.62 (s, 3H, Me$^{3'}$), 2.50 (s, 3H, Me^5), 2.41 (s, 3H, Me-

p-cym), 1.68 (s, 3H, Me$^{5'}$), 1.24 (d, J_{HH} = 6.7 Hz, 3H, ^{i}Pr-*p*-cym), 1.10 (d, J_{HH} = 6.7 Hz, 3H, ^{i}Pr-*p*-cym). ^{13}C{^{1}H}-NMR (101 MHz, CDCl$_3$) δ: 159.3–126.3 (C$^{3,3'}$,C$^{5,5'}$, quinoline group and quaternary carbons of *p*-cym), 109.8, 109.5 (C$^{4,4'}$), 110.8–80.1 (Ar-*p*-cym), 70.4, 70.3 (C^a and *C*H-OH), 31.4 (CH, ^{i}Pr-*p*-cym), 23,6, 22.8 (Me, ^{i}Pr-*p*-cym), 18.5 (Me, *p*-cym), 18.7 (Me^3), 17.5 (Me$^{3'}$), 17.3 (Me^5), 11.7 (Me^5). UV–vis: maximum absorbance at 207 nm. Elemental analysis calculated (%) for C$_{31}$H$_{37}$Cl2N$_5$ORu: C, 55.77; H, 5.59; N,10.49; found C, 55.90; H, 5.70; N, 10.48.

3.2. X-ray crystallography characterization

Prismatic crystals for RUSCO-2 and RUSCO-3 were mounted on a mitogen mount and used for data collection on a Bruker D8 Venture with a Photon II detector equipped with graphite monochromated MoKα radiation (λ = 0.71073 Å) (Bruker Apex2, Bruker AXS Inc., Madison, WI, USA, 2004). The data reduction was performed with the APEX2 software and corrected for absorption using SADABS [60]. Crystal structures were solved by SHELXT program [61] and refined by full-matrix least-squares on F2 including all reflections using anisotropic displacement parameters by means of the OLEX2 and SHELX crystallographic package [61,62]. Final R(F), wR(F2), and goodness of fit agreement factors, details on the data collection and analysis can be found in Table S1 of the Supporting Information.

3.3. Uptake studies

3.3.1. Spectral equipment and measurements

Steady-state fluorescence (SSF) spectra were recorded on an FLS920 spectrofluorometer (Edinburgh Instruments) equipped with an MCP-PMT (microchannel plate-photomultiplier tube) detector (R3809 model) and a TCSPC (time-correlated single photon counting) data acquisition card (TCC900 model). A Xe lamp of 450 W was used as the light source for SSF spectra, and a sub-nanosecond pulsed Light-Emitting Diode, EPLED-360 (Edinburgh Photonics), was employed as a light source for Time-resolved fluorescence decays (TRF). A TLC 50 temperature-controlled cuvette holder (Quantum Northwest) was used to keep the temperature at 25 °C during the spectra acquisition. Excitation and emission slits were both fixed at 4 nm, the step 1 nm and the dwell time was 0.1 s. The excitation wavelength (λex) was 368 nm, emission wavelength (λem) was 520 nm and the Δλem was 10 nm. All measurements were performed using a 10 mm quartz cuvette (Hellma Analytics).

Solutions of RUSCO-3 (10 μM) were prepared in pH 7.4 PBS solvent from stock solution (1 mM) of RUSCO-3 in DMSO solvent.

The fluorescence intensity decay, I(t), was fitted to the following multiexponential function using an iterative least-squares fit method.

$$I(t) = \sum_{i=1}^{n} \alpha_i exp(-t/\tau_i) \tag{1}$$

where αi and τi are the amplitude and lifetime for each ith term. The mean lifetime of the decay was then calculated as:

$$\tau_m = \frac{\sum_{i=1}^{n} \alpha_i \tau_i^2}{\sum_{i=1}^{n} \alpha_i \tau_i} \tag{2}$$

3.3.2. Cell cultures for FLIM microscopy

Breast cancer cells MCF7 were grown in Dulbecco's modified Eagle medium (DMEM) without phenol red. Each medium was supplemented with 10% inactivated fetal bovine serum, 1% L-glutamine, 1% penicillin/streptomycin. Cell cultures were incubated at 37 °C in a saturated humidity atmosphere with 5% of CO$_2$. For FLIM experiments, cells were seeded onto 20 mm square glass cover slides into 6-well plate and cultured (5 × 10^4 cells per plate) at 37 °C in a 5% CO$_2$ humidified atmosphere with DMEM medium without phenol red. After 24 h RUSCO-3 (10 μM) was added to the cell and incubated for 1 and 8 h.

For colocalization experiments, cells were incubated with DMEM medium without phenol red with RUSCO-3 (10 μM) for 24 h. The medium is then removed, three washes are carried out with PBS and DMEM medium without phenol red and then mitotracker deep red FM (Thermofisher) (1 nM) is added and incubated for 10 min. Finally, the medium is removed and washed again with PBS and the images are recorded in FLIM.

3.3.3. Fluorescence Lifetime Imaging of cells

Fluorescence lifetime images were recorded with a MicroTime 200 microscope (PicoQuant) equipped with a TCSPC card and two TAU-SPAD-100 avalanche photodiode detectors. A 375 nm and 637 nm pulsed diode lasers (LDH-D-C-375, 637 PicoQuant) were used as excitation source at 10 MHz repetition rate and a power of ~0.4 μW. The emission was recorded with long-pass filter (−519/19 LP). 80 × 80 μm regions were scanned with 156 nm/pixel spatial resolution and 2 ms of dwell time. FLIM images were processed using SymphoTime64 software (PicoQuant). The lifetime distribution histograms were obtained from FLIM images and were fitted to Gaussian curve. The FLIM images were smoothed over 200 nm for clarity of presentation. The emission spectra and the histograms were averaged over 3 independent measurements. For colocalization experiments, firstly, the signal emitted by the mitotracker upon excitation at 637 nm is recorded using the specific conditions of the compound (λem = 650–725 nm, 690/70 bandpass filter), and then an additional image is recorded with the emission of RUSCO-3 upon excitation at 375 nm under its specific conditions (λem >405 nm, 405 bandpass filter). Two images were taken from each group of cells (one corresponding to the mitotracker and the other to RUSCO-3), using three different cell groups as samples (6 photos in total).

3.4. Biological assays

The compounds were dissolved in dimethyl sulfoxide (DMSO) before performing each experiment. The maximal concentration used was 20 μM, due to limited water solubility; cisplatin was tested up to 14 μM. The same volume of solvent was added to control conditions and did not exceed 0.25% *v*/v.

3.4.1. Cell culture studies

The cell lines MCF7, SKBR3, BT549 and MDA-MB-231, the immortalized non-transformed keratinocyte cell line HaCaT and the immortalized human embryonic kidney cell line HEK 293 were acquired in ATCC. All lines were grown in DMEM containing 10% fetal bovine serum (FBS) and were supplemented with 100 U/mL penicillin, 5 mM L-glutamine, 100 μg/mL streptomycin at 37 °C and 5% CO2 (Sigma-Aldrich, St. Louis, MO, USA). Cisplatin was purchased from Accord Healthcare (the United Kingdom. MA).

3.4.2. MTT metabolization assays

For viability assessment of L1-L5 and RUSCO-1-RUSCO-5, cell proliferation was assayed by MTT (3-(4, 5-dimethylthiazol-2-yl)-2, 5 diphenyltetrazolium bromide) (Sigma Aldrich). Cell lines were plated at 5.000 cells per well in 96-multiwell plates. 24 h later, the cells were treated at correspondent doses of the drugs for 72 h. After that, the medium was aspirated and phenol red-free DMEM with MTT 0.5 mg/mL was added for 15 min in growth conditions. The medium was removed and MTT crystals were solubilized with 0.1 mL of dimethyl sulfoxide (DMSO) (Sigma-Aldrich) and evaluated at an absorbance of 555 nm in a multiwell plate reader.

3.4.3. Generation of ROS species

The fluorescence intensity related to the generation of ROS was measured with a FLUOstar OPTIMA microplate reader. 2′,7′-

dichlorodihydrofluorescein diacetate (H2DCFDA) from Sigma Aldrich was used as the ROS indicator. MCF7 cell line was plated at 2000 cells per well in 96-multiwell plates and incubated for 24 h at 37 °C and 5% of CO2. After that, the medium was aspirated, and the cells were treated at 3 μM of each RUSCO compound and at 8 μM of H_2O_2 as the positive control. 24 h later, the medium was removed, and the cells were washed with PBS two times. 2′,7′-dichlorodihydrofluorescein diacetate was then added at a final concentration of 10 μM in PBS. The plate was incubated 30 min and the fluorescence intensity was recorded at 520 nm.

3.4.4. Statistical analysis

The in vitro experiments data are the average of three independent experiments performed in triplicate, with error bars showing the standard deviation of the triplicates. To determine if there are statistical differences, a Student's *t*-test was performed comparing the mean cytotoxicity of each RUSCO at 4 μM with UNICAM-1 per cell line. The values for the statistical analyses are: *, $p \leq 0.05$; **, $p \leq 0.01$; ***, $p \leq 0.001$.

4. Conclusions

Metallodrugs are a well-established group of chemotherapeutic agents for the treatment of cancer. Most combination therapies include platinum-based agents. However, platinum-based therapies often develop resistance and display severe side effects. In recent years, the biological properties and anticancer potential of ruthenium compounds have been intensively investigated, nevertheless metallodrug discovery still relies heavily on the screening of compound libraries. Rational design of the ruthenium metallodrugs structure and elucidation of structure-activity relations is fundamental to improving the pharmacological profile of the therapeutic agents. In this sense, heteroscorpionate ligands are prone to stabilize from early to late translation metals, being potential candidates as building blocks for the next generation of novel metallodrugs. To do so, several ruthenium-based metallodrugs were obtained, fully characterized, and assessed as antitumoral agents against a panel of representative breast cancer cells. In particular, the derivative RUSCO-2 showed promising selectivity, as it preserved higher cytotoxicity than cisplatin against TNBC cells, being less toxic in non-transformed cells.

RUSCO-2 exhibited higher cytotoxicity within a panel of breast cancer cells, representing the different subtypes of breast cancer. In vitro, RUSCO-2 demonstrated a better antitumor profile compared to the reference drug cisplatin and UNICAM-1. However, nonspecific cytotoxicity effects on non-tumoral cells were also observed, similar to those seen with cisplatin therapy. Despite attempts to establish a relationship between structure and activity, such efforts were unsuccessful. After conducting stability studies, ROS generation studies, and the estimation of the lipophilicity values, the higher cytotoxicity of RUSCO-2 could not be attributed. RUSCO-2 is not the most lipophilic compound of the series, does not exhibit ROS generation, and shows similar solubility in water as well as stability in organic solvents or simulated biological media compared to its counterparts. Identifying a direct relationship between cytotoxic activity and the chemical structure of a drug is challenging. Numerous factors including physical and chemical properties of the drugs, affinity for the drug target, or potential interactions with other biomacromolecules could be involved in the antitumor activity of these compounds.

Results from uptake studies carried out on RUSCO-3, as a proof of concept, may reveal several major phenomena for this family of derivatives. First, the uptake of RUSCO-3 is rapid at short incubation times and is evenly distributed in the cytoplasm. Second, no significant changes in the overall average lifetime distribution histograms are observed over time in the different images, indicating that is not a prodrug and that the incorporation of the heteroscorpionate ligand protects it from aqueous processes, conversion in another entity, or the loss of the chloride group. Third, two different populations of RUSCO-3

are observed in the cytoplasm, one probably due to the free compound and the other due to its accumulation in the hydrophobic zones of the endoplasmic reticulum by interaction with macromolecules or inside lipid droplets. Finally, RUSCO-3 scarcely reach the cell nucleus, ruling out a mechanism of action based on DNA targeting in any way, as it has been broadly reported for other metallodrugs [63].

While further rational modification of the ligand structure is required together with further biological studies to ascertain the mechanism of action, this work shows the potential of heteroscorpionate ligands in both high throughputs testing and the rational design of new anticancer metallodrugs as plausible therapeutic options for breast cancer therapy.

CRediT authorship contribution statement

Elena Domínguez-Jurado: Methodology, Investigation. **Consuelo Ripoll:** Investigation, Formal analysis, Data curation. **Agustín Lara-Sánchez:** Writing – review & editing, Supervision, Resources. **Alberto Ocaña:** Writing – review & editing, Resources. **Iñigo J. Vitórica-Yrezábal:** Investigation, Formal analysis. **Iván Bravo:** Writing – original draft, Supervision, Software, Methodology, Data curation, Conceptualization. **Carlos Alonso-Moreno:** Writing – review & editing, Writing – original draft, Validation, Supervision, Resources, Project administration, Investigation, Funding acquisition, Conceptualization.

Declaration of competing interest

Carlos Alonso Moreno reports financial support was provided by Spain Ministry of Science and Innovation. Carlos Alonso Moreno reports financial support was provided by Junta de Comunidades de Castilla-La Mancha Consejería de Educación Cultura y Deportes. Alberto reports financial support was provided by Carlos III Health Institute.

Data availability

No data was used for the research described in the article.

Appendix A. Supplementary data

Crystallographic data table, NMR solution characterization, clogP estimation, stability studies of compound RUSCO-1-RUSCO-5, and dose-response curves for RUSCO-1-RUSCO-5 in a panel of breast cancer tumour cells are depicted in the Supporting Information. CCDC 2277792-2277793 contain the supplementary crystallographic data for this paper. These data can be obtained free of charge via www.ccdc.cam.ac.uk/data_request/cif, or by emailing data_request@ccdc.cam.ac.uk, or

by contacting The Cambridge Crystallographic Data Centre, 12 Union Road, Cambridge CB2 1EZ, UK; fax: +44 1223 336033. See doi:https://doi.org/10.1039/x0xx00000x Supplementary data to this article can be found online at https://doi.org/10.1016/j.jinorgbio.2024.112486.

References

[1] C. Pettinari, R. Pettinari, Metal derivatives of poly(pyrazolyl)alkanes: II. Bis (pyrazolyl)alkanes and related systems, Coord. Chem. Rev. 249 (5) (2005) 663–691, https://doi.org/10.1016/j.ccr.2004.08.017.

[2] A. Otero, J. Fernández-Baeza, A. Lara-Sánchez, J. Tejeda, L.F. Sánchez-Barba, Recent advances in the design and coordination chemistry of Heteroscorpionate ligands bearing Stereogenic Centres, Eur. J. Inorg. Chem. 2008 (34) (2008) 5309–5326, https://doi.org/10.1002/ejic.200800710.

[3] A. Otero, J. Fernández-Baeza, A. Lara-Sánchez, L.F. Sánchez-Barba, Metal complexes with Heteroscorpionate ligands based on the Bis(Pyrazol-1-Yl)methane moiety: catalytic chemistry, Coord. Chem. Rev. 257 (11) (2013) 1806–1868, https://doi.org/10.1016/j.ccr.2013.01.027.

[4] C.J. Carrano, A family of Homo- and Heteroscorpionate ligands: applications to bioinorganic chemistry, Eur. J. Inorg. Chem. 2016 (15–16) (2016) 2377–2390, https://doi.org/10.1002/ejic.201501476.

[5] H.R. Bigmore, S.R. Dubberley, M. Kranenburg, S.C. Lawrence, A.J. Sealey, J. D. Selby, M.A. Zuideveld, A.R. Cowley, P. Mountford, A remarkable inversion of structure–activity dependence on imido n-substituents with varying co-ligand topology and the synthesis of a new borate-free zwitterionic polymerisation catalyst, Chem. Commun. 4 (2006) 436–438, https://doi.org/10.1039/B514467A.

[6] H. Kopf, B. Holzberger, C. Pietraszuk, E. Hübner, N. Burzlaff, Neutral ruthenium carbene complexes bearing N,N,O heteroscorpionate ligands: syntheses and activity in metathesis reactions, Organometallics 27 (22) (2008) 5894–5905, https://doi.org/10.1021/om8006129.

[7] G. Türkoglu, S. Tampier, F. Strinitz, F.W. Heinemann, E. Hübner, N. Burzlaff, Ruthenium carbonyl complexes bearing Bis(Pyrazol-1-Yl)Carboxylato ligands, Organometallics 31 (6) (2012) 2166–2174, https://doi.org/10.1021/om2009155.

[8] D.M. Lyubov, A.V. Cherkasov, G.K. Fukin, A.A. Trifonov, Selective intermolecular C–H bond activation: a straightforward synthetic approach to heteroalkyl yttrium complexes containing a bis(pyrazolyl)methyl ligand, Organometallics 35 (2) (2016) 126–137, https://doi.org/10.1021/acs.organomet.5b00883.

[9] A. Otero, A. Lara-Sánchez, C. Nájera, J. Fernández-Baeza, I. Márquez-Segovia, J. A. Castro-Osma, J. Martínez, L.F. Sánchez-Barba, A.M. Rodríguez, New highly active heteroscorpionate-containing lutetium catalysts for the hydroamination of aminoalkenes: isolation and structural characterization of a dipyrrolidinide–lutetium complex, Organometallics 31 (6) (2012) 2244–2255, https://doi.org/10.1021/om2011672.

[10] F. de la Cruz-Martínez, Martínez de Sarasa, M. Buchaca, J. Martínez, J. Tejeda, J. Fernández-Baeza, C. Alonso-Moreno, A.M. Rodríguez, J.A. Castro-Osma, A. Lara-Sánchez, Bimetallic zinc catalysts for ring-opening copolymerization processes, Inorg. Chem. 59 (12) (2020) 8412–8423.

[11] J.A. Castro-Osma, C. Alonso-Moreno, J.C. García-Martinez, J. Fernández-Baeza, L. F. Sánchez-Barba, A. Lara-Sánchez, A. Otero, Ring-opening (ROP) versus ring-expansion (REP) polymerization of ε-Caprolactone to give linear or cyclic Polycaprolactones, Macromolecules 46 (16) (2013) 6388–6394.

[12] J. Martínez, M.M.S. Buchaca, F. Cruz-Martínez, C. Alonso-Moreno, L.F. Sánchez-Barba, J. Fernandez-Baeza, A.M. Rodríguez, A. Rodríguez-Diéguez, J.A. Castro-Osma, A. Otero, A. Lara-Sánchez, Versatile Organoaluminium catalysts based on Heteroscorpionate ligands for the preparation of polyesters, Dalton Trans. 47 (22) (2018) 7471–7479, https://doi.org/10.1039/C8DT01553H.

[13] J. Martínez, F. de la Cruz-Martínez, M.A. Gaona, E. Pinilla-Peñalver, J. Fernández-Baeza, A.M. Rodríguez, J.A. Castro-Osma, A. Otero, A. Lara-Sánchez, Influence of the Counterion on the synthesis of cyclic carbonates catalyzed by bifunctional aluminum complexes, Inorg. Chem. 58 (5) (2019) 3396–3408, https://doi.org/10.1021/acs.inorgchem.8b03475.

[14] M.A. Andrade, L.M.D.R.S. Martins, Novel chemotherapeutic agents - the contribution of scorpionates, Curr. Med. Chem. 26 (41) (2019) 7452–7475.

[15] E.J. Anthony, E.M. Bolitho, H.E. Bridgewater, O.W.L. Carter, J.M. Donnelly, C. Imberti, E.C. Lant, F. Lermyte, R.J. Needham, M. Palau, P.J. Sadler, H. Shi, F.-X. Wang, W.-Y. Zhang, Z. Zhang, Metallodrugs are unique: opportunities and challenges of discovery and development, Chem. Sci. 11 (48) (2020) 12888–12917, https://doi.org/10.1039/d0sc04082g.

[16] S.M. Meier-Menches, C. Gerner, W. Berger, C.G. Hartinger, B.K. Keppler, Structure-activity relationships for ruthenium and osmium anticancer agents - towards clinical development, Chem. Soc. Rev. 47 (3) (2018) 909–928, https://doi.org/10.1039/c7cs00332c.

[17] A. Levina, A.R.M. Chetcuti, P.A. Lay, Controversial role of transferrin in the transport of ruthenium anticancer drugs, Biomolecules 12 (9) (2022) 1319, https://doi.org/10.3390/biom12091319.

[18] M. Hanif, C.G. Hartinger, Anticancer Metallodrugs: where is the next cisplatin? Future Med. Chem. 10 (6) (2018) 615–617, https://doi.org/10.4155/fmc-2017-0317.

[19] I. Pötsch, D. Baier, B.K. Keppler, W. Berger, Challenges and Chances in the Preclinical to Clinical Translation of Anticancer Metallodrugs, 2019, pp. 308–347, https://doi.org/10.1039/9781788016452-00308.

[20] R. Paprocka, M. Wiese-Szadkowska, S. Janciauskiene, T. Kosmalski, M. Kulik, A. Helmin-Basa, Latest developments in metal complexes as anticancer agents,

[21] Theralase Inc, A Phase II Clinical Study of Intravesical Photodynamic Therapy in Patients With BCG-Unresponsive Non-Muscle Invasive Bladder Cancer ("NMIBC") Or Patients Who Are Intolerant to BCG Therapy ("Study").; Clinical trial registration NCT03945162. clinicaltrials.gov, 2021. https://clinicaltrials.gov/ct2/show/NCT03945162 (accessed 2021-07-06).

[22] Bold Therapeutics, Inc, A Phase 1b/2a Dose Escalation Study of BOLD-100 in Combination With FOLFOX Chemotherapy in Patients With Advanced Solid Tumours; Clinical trial registration NCT04421820. clinicaltrials.gov, 2023. https://clinicaltrials.gov/study/NCT04421820 (accessed 2023-01-01).

[23] R.E. Aird, J. Cummings, A.A. Ritchie, M. Muir, R.E. Morris, H. Chen, P.J. Sadler, D. I. Jodrell, In vitro and in vivo activity and cross resistance profiles of novel ruthenium (II) organometallic Arene complexes in human ovarian Cancer, Br. J. Cancer 86 (10) (2002) 1652–1657, https://doi.org/10.1038/sj.bjc.6600290.

[24] Q. Peña, A. Wang, O. Zaremba, Y. Shi, H.W. Scheeren, J.M. Metselaar, F. Kiessling, R.M. Pallares, S. Wuttke, T. Lammers, Metallodrugs in Cancer nanomedicine, Chem. Soc. Rev. 51 (7) (2022) 2544–2582, https://doi.org/10.1039/D1CS00468A.

[25] L. Côrte-Real, R.G. Teixeira, P. Gírio, E. Comsa, A. Moreno, R. Nasr, H. Baubichon-Cortay, F. Avecilla, F. Marques, M.P. Robalo, P. Mendes, J.P.P. Ramalho, M. H. Garcia, P. Falson, A. Valente, Methyl-cyclopentadienyl ruthenium compounds with 2,2'-Bipyridine derivatives display strong anticancer activity and multidrug resistance potential, Inorg. Chem. 57 (8) (2018) 4629–4639, https://doi.org/10.1021/acs.inorgchem.8b00358.

[26] S. Swaminathan, J. Haribabu, N. Balakrishnan, P. Vasanthakumar, R. Karvembu, Piano stool Ru(II)-Arene complexes having three Monodentate legs: a comprehensive review on their development as anticancer Therapeutics over the past decade, Coord. Chem. Rev. 459 (2022) 214403, https://doi.org/10.1016/j.ccr.2021.214403.

[27] J.P.C. Coverdale, T. Laroiya-McCarron, I. Romero-Canelón, Designing ruthenium anticancer drugs: what have we learnt from the key drug candidates? Inorganics 7 (3) (2019) 31, https://doi.org/10.3390/inorganics7030031.

[28] G. Golbaghi, A. Castonguay, Rationally designed ruthenium complexes for breast Cancer therapy, Molecules 25 (2) (2020) 265, https://doi.org/10.3390/molecules25020265.

[29] A. Rilak Simović, R. Masnikosa, I. Bratsos, E. Alessio, Chemistry and reactivity of ruthenium(II) complexes: DNA/protein binding mode and anticancer activity are related to the complex structure, Coord. Chem. Rev. 398 (2019) 113011, https://doi.org/10.1016/j.ccr.2019.07.008.

[30] C.S. Allardyce, P.J. Dyson, D.J. Ellis, S.L. Heath, [Ru(H6-p-cymene)Cl2(Pta)] (Pta = 1,3,5-Triaza-7-Phosphatricyclo- [3.3.1.1]Decane): a water soluble compound that exhibits pH dependent DNA binding providing selectivity for diseased cells, Chem. Commun. 15 (2001) 1396–1397, https://doi.org/10.1039/B104021A.

[31] C. Scolaro, A. Bergamo, L. Brescacin, R. Delfino, M. Cocchietto, G. Laurenczy, T. J. Geldbach, G. Sava, P.J. Dyson, In vitro and in vivo evaluation of ruthenium(II)− Arene PTA complexes, J. Med. Chem. 48 (12) (2005) 4161–4171, https://doi.org/10.1021/jm050015d.

[32] E. Alessio, L. Messori, NAMI-A and KP1019/1339, two iconic ruthenium anticancer drug candidates face-to-face: a case story in medicinal inorganic chemistry, Mol. Basel Switz. 24 (10) (2019) E1995, https://doi.org/10.3390/molecules24101995.

[33] C.G. Hartinger, M.A. Jakupec, S. Zorbas-Seifried, M. Groessl, A. Egger, W. Berger, H. Zorbas, P.J. Dyson, B.K. Keppler, KP1019, a new redox-active anticancer agent – preclinical development and results of a clinical phase I study in tumor patients, Chem. Biodivers. 5 (10) (2008) 2140–2155, https://doi.org/10.1002/cbdv.200890195.

[34] V. Corrales Sanchez, C. Nieto-Jiménez, J.A. Castro-Osma, F. De Andrés, P. J. Pacheco-Liñán, I. Bravo, N. Rodriguez Farinas, E. Niza, E. Domínguez-Jurado, A. Lara-Sánchez, Screening and preliminary biochemical and biological studies of [RuCl (p-cymene)(N, N-Bis (Diphenylphosphino)-Isopropylamine)][BF4] in breast Cancer models, ACS Omega 4 (8) (2019) 13005–13014.

[35] L.M. Broomfield, C. Alonso-Moreno, E. Martin, A. Shafir, I. Posadas, V. Ceña, J. A. Castro-Osma, Aminophosphine ligands as a privileged platform for development of Antitumoral ruthenium(II) Arene complexes, Dalton Trans. 46 (46) (2017) 16113–16125, https://doi.org/10.1039/C7DT03369A.

[36] E. Domínguez-Jurado, F.J. Cimas, J.A. Castro-Osma, A. Juan, A. Lara-Sánchez, A. Rodríguez-Diéguez, A. Shafir, A. Ocaña, C. Alonso-Moreno, Tuning the cytotoxicity of Bis-Phosphino-amines ruthenium (II) Para-cymene complexes for clinical development in breast Cancer, Pharmaceutics 13 (10) (2021) 1559.

[37] N. Mendes, F. Tortosa, A. Valente, F. Marques, A. Matos, T.S. Morais, A.I. Tomaz, F. Gärtner, M.H. Garcia, In vivo performance of a ruthenium-cyclopentadienyl compound in an Orthotopic triple negative breast Cancer model, Anticancer Agents Med Chem. 17 (1) (2017) 126–136.

[38] T.S. Morais, F. Marques, P.J.A. Madeira, M.P. Robalo, M.H. Garcia, Design and anticancer properties of new water-soluble ruthenium–cyclopentadienyl complexes, Pharmaceuticals 15 (7) (2022) 862, https://doi.org/10.3390/ph15070862.

[39] G. Golbaghi, I. Pitard, M. Lucas, M.M. Haghdoost, Y.L. de Los Santos, N. Doucet, S. A. Patten, J.T. Sanderson, A. Castonguay, Synthesis and biological assessment of a ruthenium(II) cyclopentadienyl complex in breast Cancer cells and on the development of zebrafish embryos, Eur. J. Med. Chem. 188 (2020) 112030, https://doi.org/10.1016/j.ejmech.2019.112030.

[40] C. Pettinari, R. Pettinari, N. Xhaferai, G. Giambastiani, A. Rossin, L. Bonfili, A. Maria Eleuteri, M. Cuccioloni, Binuclear 3,3',5,5'-Tetramethyl-1H,H-4,4'-Bipyrazole Ruthenium(II) Complexes: Synthesis, Characterization and Biological Studies, Inorganica Chim. Acta 513 (2020) 119902, https://doi.org/10.1016/j.ica.2020.119902.

[41] M. Montani, G.V.B. Pazmay, A. Hysi, G. Lupidi, R. Pettinari, V. Gambini, M. Tilio, F. Marchetti, C. Pettinari, S. Ferraro, M. Iezzi, C. Marchini, A. Amici, The water soluble ruthenium(II) organometallic compound [Ru(p-cymene)(Bis(3,5 Dimethylpyrazol-1-Yl)methane)cl]cl suppresses triple negative breast Cancer growth by inhibiting tumor infiltration of regulatory T cells, Pharmacol. Res. 107 (2016) 282–290, https://doi.org/10.1016/j.phrs.2016.03.032.

[42] S.K. Tripathy, R.K. Surada, R.K. Manne, S.M. Mobin, M.K. Santra, S. Patra, Synthesis, Characterisation and Biological Activities of [(p-Cym)RuX(Pz4lut)]N+ and [{(p-Cym)RuX}2(μ-Pz4lut)]N+ (X = Cl, H2O and Pz4lut = α,α,Α′,Α′-Tetra (Pyrazol-1-Yl)-2,6-Lutidine), Dalton Trans. 42 (39) (2013) 14081–14091, https://doi.org/10.1039/C3DT51275D.

[43] R.A. Khan, F. Arjmand, S. Tabassum, M. Monari, F. Marchetti, C. Pettinari, Organometallic ruthenium(II) Scorpionate as topo IIα inhibitor; in vitro binding studies with DNA, HPLC analysis and its anticancer activity, J. Organomet. Chem. 771 (2014) 47–58, https://doi.org/10.1016/j.jorganchem.2014.05.013.

[44] N. Nayeem, M. Contel, Exploring the potential of Metallodrugs as chemotherapeutics for triple negative breast Cancer, Chem. A Eur. J. 27 (35) (2021) 8891–8917, https://doi.org/10.1002/chem.202100438.

[45] M. Frik, A. Martínez, B.T. Elie, O. Gonzalo, D. Ramírez de Mingo, M. Sanaú, R. Sánchez-Delgado, T. Sadhukha, S. Prabha, J.W. Ramos, I. Marzo, M. Contel, In vitro and in vivo evaluation of water-soluble Iminophosphorane ruthenium(II) compounds. A potential chemotherapeutic agent for triple negative breast Cancer, J. Med. Chem. 57 (23) (2014) 9995–10012, https://doi.org/10.1021/jm5012337.

[46] J. Shen, H.-C. Kim, J. Wolfram, C. Mu, W. Zhang, H. Liu, Y. Xie, J. Mai, H. Zhang, Z. Li, M. Guevara, Z.-W. Mao, H. Shen, A liposome encapsulated ruthenium Polypyridine complex as a Theranostic platform for triple-negative breast Cancer, Nano Lett. 17 (5) (2017) 2913–2920, https://doi.org/10.1021/acs.nanolett.7b00132.

[47] L. Zeng, P. Gupta, Y. Chen, E. Wang, L. Ji, H. Chao, Z.-S. Chen, The development of anticancer ruthenium(II) complexes: from single molecule compounds to nanomaterials, Chem. Soc. Rev. 46 (19) (2017) 5771–5804, https://doi.org/10.1039/C7CS00195A.

[48] A. Otero, J. Fernández-Baeza, J. Tejeda, A. Lara-Sánchez, M. Sánchez-Molina, S. Franco, I. López-Solera, A.M. Rodríguez, L.F. Sánchez-Barba, S. Morante-Zarcero, A. Garcés, On the search for NNO-donor Enantiopure Scorpionate ligands and their coordination to group 4 metals, Inorg. Chem. 48 (12) (2009) 5540–5554, https://doi.org/10.1021/ic900352e.

[49] O. Sari, A. Schüttler, P. Lönnecke, P.J. Bednarski, E. Hey-Hawkins, M. Karakus, Synthesis, structure and in vitro anticancer activity of ruthenium(II) and platinum (II) complexes with chiral Aminophosphine ligands, Transit. Met. Chem. 46 (4) (2021) 299–305, https://doi.org/10.1007/s11243-020-00446-0.

[50] J.-M. delMoral-Sanchez, I. Gonzalez-Alvarez, M. Gonzalez-Alvarez, A. Navarro, M. Bermejo, Classification of WHO essential Oral medicines for children applying a provisional pediatric biopharmaceutics classification system, Pharmaceutics 11 (11) (2019) 567, https://doi.org/10.3390/pharmaceutics11110567.

[51] The International Pharmacopoeia. https://digicollections.net/phint/2022/index.html#p/home, 2022.

[52] W.D.J. Tremlett, D.M. Goodman, T.R. Steel, S. Kumar, A. Wieczorek-Błauż, F. P. Walsh, M.P. Sullivan, M. Hanif, C.G. Hartinger, Design concepts of half-Sandwich Organoruthenium anticancer agents based on bidentate bioactive ligands, Coord. Chem. Rev. 445 (2021) 213950, https://doi.org/10.1016/j.ccr.2021.213950.

[53] T.R. Steel, F. Walsh, A. Wieczorek-Błauż, M. Hanif, C.G. Hartinger, Monodentately-coordinated bioactive moieties in multimodal half-Sandwich Organoruthenium anticancer agents, Coord. Chem. Rev. 439 (2021) 213890, https://doi.org/10.1016/j.ccr.2021.213890.

[54] I. Bravo, C. Alonso-Moreno, I. Posadas, J. Albaladejo, F. Carrillo-Hermosilla, V. Ceña, A. Garzón, I. López-Solera, L. Romero-Castillo, Phenyl-guanidine derivatives as potential therapeutic agents for glioblastoma Multiforme: catalytic syntheses, cytotoxic effects and DNA affinity, RSC Adv. 6 (10) (2016) 8267–8276, https://doi.org/10.1039/C5RA17920C.

[55] Molinspiration Cheminformatics. https://www.molinspiration.com/, 2024 (accessed 2023-12-27).

[56] A. Baranova, M. Krasnoselskyi, V. Starikov, S. Kartashov, I. Zhulkevych, V. Vlasenko, K. Oleshko, O. Bilodid, M. Sadchikova, Y. Vinnyk, Triple-negative breast Cancer: current treatment strategies and factors of negative prognosis, J. Med. Life 15 (2) (2022) 153–161, https://doi.org/10.25122/jml-2021-0108.

[57] M. Musthafa, R. Konakanchi, R. Ganguly, P. Pandikumar, A. Sreekanth, Synthesis, characterization, in silico and in vitro biological activity studies of Ru(II) (H6-p-cymene) complexes with novel N-Dibenzosuberene substituted Aroyl Selenourea exhibiting se type coordination, Res. Chem. Intermed. 46 (8) (2020) 3853–3877, https://doi.org/10.1007/s11164-020-04177-w.

[58] P.J. Pacheco-Liñán, C. Martín, C. Alonso-Moreno, A. Juan, D. Hermida-Merino, A. Garzón-Ruíz, J. Albaladejo, M.V. Auweraer, B. Cohen, I. Bravo, The role of water and influence of hydrogen bonding on the self-assembly aggregation induced emission of an anthracene-guanidine-derivative, Chem. Commun. (2020) 4102–4105, https://doi.org/10.1039/d0cc00990c.

[59] J.R. Lakowicz, Principles of Fluorescence Spectroscopy, 3rd ed., Springer US, 2006 https://doi.org/10.1007/978-0-387-46312-4.

[60] G. Sheldrick, SADABS, Program for Empirical Absorption Correction of Area Detector Data, 1996.

[61] G.M. Sheldrick, Crystal structure refinement with SHELXL, Acta Crystallogr. Sect. C Struct. Chem. 71 (1) (2015) 3–8, https://doi.org/10.1107/S2053229614024218.

[62] O.V. Dolomanov, L.J. Bourhis, R.J. Gildea, J. Howard, H. Puschmann, OLEX2: a complete structure solution, refinement and analysis program, J. Appl. Cryst. 42 (2) (2009) 339–341, https://doi.org/10.1107/S0021889808042726.

[63] J. Cervinka, A. Gobbo, L. Biancalana, L. Markova, V. Novohradsky, M. Guelfi, S. Zacchini, J. Kasparkova, V. Brabec, F. Marchetti, Ruthenium(II)–Tris-Pyrazolylmethane complexes inhibit Cancer cell growth by disrupting mitochondrial calcium homeostasis, J. Med. Chem. 65 (15) (2022) 10567–10587, https://doi.org/10.1021/acs.jmedchem.2c00722.